

Photoluminescence efficiency of Al-rich AlGa_xN heterostructures in a wide range of photoexcitation densities over temperatures up to 550 K

S. Miasojedovas^{1,*}, P. Ščajev¹, K. Jarašiūnas¹, B. Gil² and H. Miyake³

¹*Institute of Photonics and Nanotechnology, Vilnius University, Sauletekio Avenue 3, LT 10257 Vilnius, Lithuania*

²*Laboratoire Charles Coulomb, CNRS, UMR 5221, Montpellier, France*

³*Graduate School of Regional Innovation Studies, Mie University, 1577 Kurimamachiya, Tsu, Mie 514-8507, Japan*



(Received 3 July 2019; revised 8 May 2020; accepted 11 June 2020; published 1 July 2020)

Time-resolved photoluminescence and light-induced transient grating techniques were applied for the comparative investigation of the evolution of the internal quantum efficiency and of the carrier diffusion in an Al_xGa_{1-x}N silicon-doped epilayer and Al_xGa_{1-x}N MQWs ($x > 0.6$). The experiments were performed between 80 and 550 K under various densities of excitation from $1 \mu\text{J cm}^{-2}$ to 1 mJ cm^{-2} . The decrease of the photoluminescence efficiency measured at high excitations is quantitatively correlated to the increase of the diffusion coefficients of carriers and to the increase of their nonradiative recombination rate. We evidence the reduction of the density of localized excitons with increasing both excitation density and temperature. The decrease of the excitation-dependent lifetime is less pronounced than the corresponding drop of the time-integrated photoluminescence efficiency. This is dominated by the thermal dissociation of excitons. At the lowest excitation densities, the excitons are captured to vacancy complexes. When increasing the excitation density, the ionization of excitons is produced, which leads to enhancing the nonradiative recombination of holes to aluminum vacancies and this simultaneously quenches the PL efficiency, due to the saturation of the bimolecular free-carrier-plasma recombination. At the initial recombination stages and under high excitation conditions we reveal diffusive recombination on dislocations. After a careful and sophisticated modeling, we establish relevant numbers for the following: (i) the free exciton binding energies, with values of 104 and 140 meV in the MQWs and in the layer respectively; (ii) the exciton localization energies, which are framed in the 12–35-meV range; (iii) the lifetimes of the localized excitons, which sit in the 2–4-ns range; (iv) the free exciton and carrier radiative recombination rate coefficients that are $r_{\text{ex}} = (0.6 \pm 0.2) \times (T/300)^{-1} \times 10^9 \text{ s}^{-1}$ and $B_{\text{rad}} = (7 \pm 1) \times (T/300)^{-3/2} \times 10^{-10} \text{ cm}^3 \text{ s}^{-1}$, respectively; (v) the capture cross section for excitons to the vacancy complex $\sigma = (2 \pm 1) \times (300/T)^2 \times 10^{-16} \text{ cm}^2$. Regarding the electron and hole capture cross sections to aluminum vacancy we found values of $(1.5 \pm 1) \times 10^{-13} \text{ cm}^2$ and $(7 \pm 1) \times 10^{-13} \text{ cm}^2$, respectively. The value of the Coulomb dislocation radius for the free-carrier recombination is established to be 12–15 nm.

DOI: [10.1103/PhysRevB.102.035201](https://doi.org/10.1103/PhysRevB.102.035201)

I. INTRODUCTION

The recent progress in the growth of aluminum-rich AlGa_xN layers and of quantum structures based on them is today boosting a lot of applications in the ultraviolet (UV). Among them are disinfection, optical data storage, plant growth, food industry, water disinfection, biological hazard prevention, excitation of fluorophores, and fabrication of various specific sensors [1–6]. Deep UV light emitting diodes (DUV-LEDs) are perfect candidates for the replacement of lamps based on mercury that are consuming high electrical power. DUV-LEDs still suffer from low quantum efficiency and further studies and development are mandatorily needed to improve them in the view of fulfilling the prescriptions of the Minamata convention on mercury. Previously applied for sterilization, the use of this toxic element in fluorescent light bulbs is prohibited starting in 2020 [7].

Previous works of such materials have revealed that carrier localization varies with the aluminum content and the evolution of the recombination rate with temperature in AlGa_xN alloys and QWs also raised a lot of questions. Therefore, in-depth understanding of them now appears of paramount importance for the design of DUV emitters [8–14] with high photoluminescence (PL) efficiency. The doping of Al_xGa_{1-x}N alloys ($x = 0.3\text{--}0.7$) [15] and of Al-rich QW wells ($x = 0.58\text{--}0.6$) [16] with Si produces an enhancement of the internal quantum efficiency (IQE). Si doping prevents the compressive strain relaxation and it contributes to the decrease of the nonradiative recombination rate. This decrease was correlated to the improvement of the well-barrier interface [16] for Si concentration up to $7 \times 10^{17} \text{ cm}^{-3}$. When further increasing the Si doping beyond such a critical value, dislocations are created with a large density [17], and this causes both PL intensity and lifetime to decrease [18], indicating a correlation, and it proves the impact of dislocations to recombination process. Time-resolved temperature-dependent PL spectroscopy of Al-rich MQWs ($x = 0.68$) [19] provided nonexponential PL decay with an initial PL decay time (here

*saulius.miasojedovas@ff.vu.lt

we define it as the time after the excitation pulse when the initial peak intensity is divided by (e) of ~ 1 ns remained unchanged up to 150–200 K, which we interpret in terms of the signature of radiative emission of excitons, from bona fide avoiding their further capture by nonradiative defects.

As most of the previous studies of Al-rich AlGaIn compounds have been performed under conditions of low and/or moderate photoexcitation densities [16,20,21] or by analyzing only time-integrated features of PL without considering the variations of the lifetimes of carriers [22], the question regarding the dynamics of recombination and regarding the droop of the PL efficiency at high carrier injection levels keeps open to date. Its answer requires complementary and deeper studies of the PL kinetics for elucidating the origin of the fast recombination transients. In the perspective of this, we studied the carrier lifetimes and the PL efficiency in the context of a wide range of excitation densities and for temperatures ranging from 80 K up to 550 K. Both complementary techniques of time-resolved PL (TRPL) and light-induced transient grating (LITG) were extensively used in order to determine the carrier lifetimes and the diffusion coefficients of the carriers [23]. By analyzing the decays of photoluminescence correlated to defects, we reveal that aluminum vacancies are the dominant nonradiative recombination centers for holes; we demonstrate that vacancy complexes reduce the quantum efficiency only at low excitations. We present the experimental correlation between the excitation-dependent decrease of PL decay times and the simultaneous increase of diffusion coefficients. We discuss the impact of these changes to the temperature-dependent and the excitation-dependent quenching of the PL efficiency.

II. SAMPLES AND TECHNIQUES

We extend here preliminary studies of the carrier dynamics performed on two AlGaIn heterostructures with high aluminum content and available in Ref. [23] to broader ranges of temperature and excitation densities. The first sample (hereafter referenced as “the AlGaIn layer”) is a 0.8- μm -thick Si-doped $\text{Al}_{0.68}\text{Ga}_{0.62}\text{N}$ layer, grown on undoped 0.2- μm -thick Al-rich AlGaIn sublayer ($x = 0.76$) predeposited on an AlN nucleation layer itself grown on c -plane sapphire. The second sample (hereafter referenced as “the MQWs”) contains Si-doped multiple quantum wells (MQWs) with 100 periods of $\text{Al}_{0.61}\text{Ga}_{0.39}\text{N}/\text{Al}_{0.70}\text{Ga}_{0.30}\text{N}$. In this case, the basic building block of these MQWs is a 1.4-nm-thin well layer embedded into 6.8-nm-thin barrier layers. The whole stacking is grown on a 0.2- μm -thick Si-doped Al-rich AlGaIn sublayer ($x = 0.76$) grown on an undoped 0.2- μm -thick Al-rich AlGaIn sublayer ($x = 0.82$ – 0.9) predeposited on an AlN nucleation layer itself grown on the c plane. Note that we select here samples with very similar average Al contents to facilitate the comparison of the physical properties of AlGaIn layers with those of MQWs ($x = 0.684$ on average). The Si concentration n_0 in the structures ($n_0 \sim 4$ – $5 \times 10^{17} \text{ cm}^{-3}$) is optimized for the efficient reduction of the compressive strain [16]. By making this choice we did not care about its impact on the localization energy of carriers [15]. The dislocation density in the samples is $1.5 \times 10^9 \text{ cm}^{-2}$. The growth procedure is

extensively detailed in Ref. [24]; the structural investigations of the MQWs can be found in Ref. [23].

The measurements of the PL and of the carrier dynamics were performed by standard means of TRPL and LITG methods, using for photoexcitation pulses of YAG : Nd^{3+} laser fifth harmonic (at a wavelength of 213 nm) having a duration $\tau_L = 20$ ps [23]. The TRPL measurements were performed using a HAMAMATSU C10627 streak camera and an Acton SP2300 monochromator. The range of excitation fluences I_0 scaled three decades from 10^{-3} mJ/cm^2 up to 1 mJ/cm^2 and they provided excess carrier density $\Delta N_0 = 10^{17}$ – 10^{20} cm^{-3} , according to the relationship $\Delta N_0 = \alpha I_0/h\nu$, where the experimental value of absorption coefficient $\alpha(213 \text{ nm}) = 1.8 \times 10^5 \text{ cm}^{-1}$ [25]. The average carrier density after the photoexcitation pulse was calculated as $\Delta N = \Delta N_0/2$ [26]. The time-dependent instantaneous LITG diffraction efficiency is written $DE(t) \sim \Delta N_0^2 \exp(-2t/\tau_G)$, with a grating decay time τ_G . It was monitored by the diffraction of a delayed probe beam having a wavelength of 1064 nm [27]. This is allowing simultaneous measurements of the recombination lifetime τ and diffusion coefficient D from the relation

$$1/\tau_G = 1/\tau + 4\pi^2 D/\Lambda^2. \quad (1)$$

Here Λ is the LITG grating period.

For the determination of the absolute value of the internal quantum efficiency η_{PL} , we performed direct measurements of the time-integrated values of the emission (I_{TIPL}) and excitation densities (I_0) at 300 K by using a PL calibration setup [28]. The measurements at $\sim 1 \text{ mJ/cm}^2$ provided $\eta_{\text{PL}} = 3.5 \pm 0.6\%$ at 300 K in the AlGaIn layer, using the following relationship [28]:

$$\eta_{\text{PL}} = I_{\text{TIPL}}F/I_0, \quad (2)$$

where

$$F = \{1 - \cos^2[\arctan(r_{\text{det}}/r)]\}/[n_g(n_g + 1)^2] \quad (3)$$

is the light extraction factor from the surface of the photoexcited AlGaIn. Our experimental conditions are such as that the collection aperture diameter $r_{\text{det}} = 3$ cm and the distance to it $r = 10$ cm. An important quantity is the refraction index at the PL emission wavelength: $n_g = 2.3$.

The experimental values of η_{PL} at 300 K allowed the extrapolation of a low-temperature PL efficiency value to a number close to 100% at 80–110 K for the conditions of low densities of photoexcitation [see Figs. 1(a) and 1(c)]. Consequently, a radiative nature can be attributed to the observed average carrier lifetime of 0.9 ns at ~ 80 K. It is in good agreement with the previously reported lifetime of 1 ns measured in the 8–180-K range for this alloy [19].

III. RESULTS AND DISCUSSION

A. Photoluminescence spectra and decays

Figures 1(a) and 1(b) depict the PL spectra of the AlGaIn layer [Fig. 1(a)] and MQWs [Fig. 1(b)] recorded under various excitation densities at 300 K. The PL spectra of the AlGaIn layer [Fig. 1(a)] display one broad band with a full width at half maximum (FWHM) ~ 240 meV centered at 245 nm

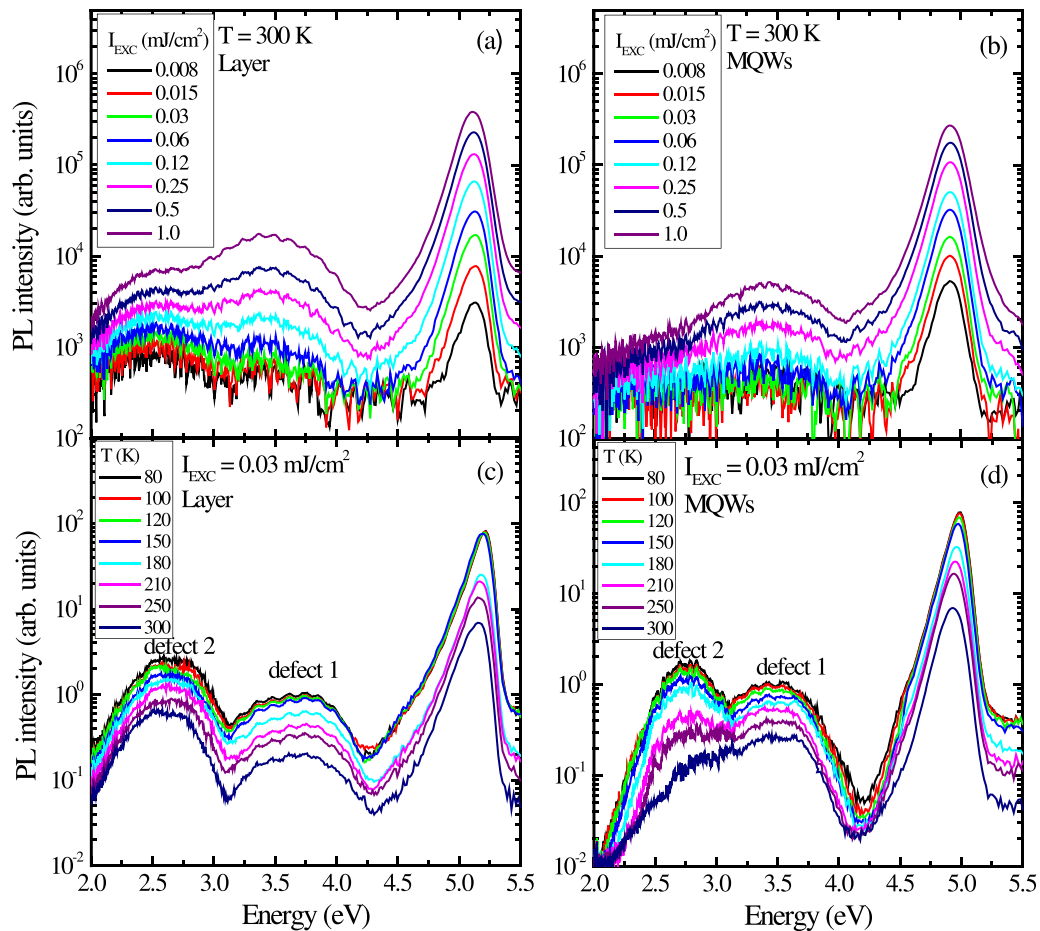


FIG. 1. Photoluminescence spectra of the $\text{Al}_{0.68}\text{Ga}_{0.32}\text{N}$ layer (a) and of the $\text{Al}_{0.61}\text{Ga}_{0.39}\text{N}/\text{Al}_{0.70}\text{Ga}_{0.30}\text{N}$ MQWs (b) against excitation intensities at 300 K. Photoluminescence spectra of $\text{Al}_{0.68}\text{Ga}_{0.32}\text{N}$ layer (c) and of $\text{Al}_{0.61}\text{Ga}_{0.39}\text{N}/\text{Al}_{0.70}\text{Ga}_{0.30}\text{N}$ MQWs (d) at various temperatures under low excitation density.

(5.06 eV) while for the MQWs, the equivalent PL band is situated at 252 nm (4.92 eV) with a similar FWHM of about 240 meV [Fig. 1(b)] [19]. The PL peak positions are almost insensitive to the density of photoexcitation: we record a blueshift of about 20 meV and an increase of FWHM of less than 7 meV with increasing the photoexcitation density. This teaches us that the localization centers correlated to fluctuations of the alloy composition are quite short-range extended, in analogy with what is found in InGaIn alloys, where ~ 10 -nm-size clusters were observed by high-resolution transmission electron microscopy (HRTEM) [29]. The fluctuations of their extensions or, said using another phrasing, their distribution of size lead to this quantum-dot-like behavior responsible for the observed broad and excitation-independent spectral shapes [30,31]. In the range of high excitation densities, the localizing centers are saturated and the near band-edge emission at high energy is due to free excitons and free carriers.

The properties of aluminum-gallium nitride alloys are intriguing. At low AlN mole fraction, AlGaIn epilayers display pronounced phase separation. With increasing AlN mole fraction, such phase separation is strongly suppressed by the formation of a spontaneous modulation of composition. The spontaneous formation of such spontaneous superlattice occurs for $x > 0.5$, as confirmed by HRTEM investigations [32]. Spontaneous superlattices (SSLs) with 0.7-nm QWs and 2-nm

barriers lead to abrupt spectral redshift and enhanced broadening. The well with fluctuation is rather large leading to an enhanced exciton localization in the layer. The latter is a cause of high modulation of composition: $x = 0.46$ in wells and $x = 0.78$ in barriers in our sample. Thus the AlGaIn layer can be considered as a superlattice $\text{Al}_{0.46}\text{Ga}_{0.64}\text{N}/\text{Al}_{0.78}\text{Ga}_{0.22}\text{N}$ for the photocreated carriers and for the modeling of its optical properties.

With increasing the temperature from 80 K to RT, the intensities of the PL spectra gradually decrease, due to the thermal dissociation of excitons [Figs. 1(c) and 1(d)]. The nonradiative recombination channels are quite efficient as for temperatures higher than 470 K, the PL from the MQWs could no longer be detected. Astonishingly we did not observe amplified spontaneous emission (ASE) in our samples: there never appeared a specific narrow PL band. Instead of this, the shapes of the spectra did not vary when increasing the photoexcitation density, and the PL decays (that we will show later) did not considerably differ spectrally. In fact we have to emphasize that a similar situation was already observed in Ref. [33]. ASE is hindered probably by the inhomogeneous fluctuations of the energies combined with the high density of states in the valence band. As indicated in Ref. [34], the thresholds for the onset of ASE for temperatures between 80 and 300 K are about 0.5–2 MW/cm² [34], which correspond

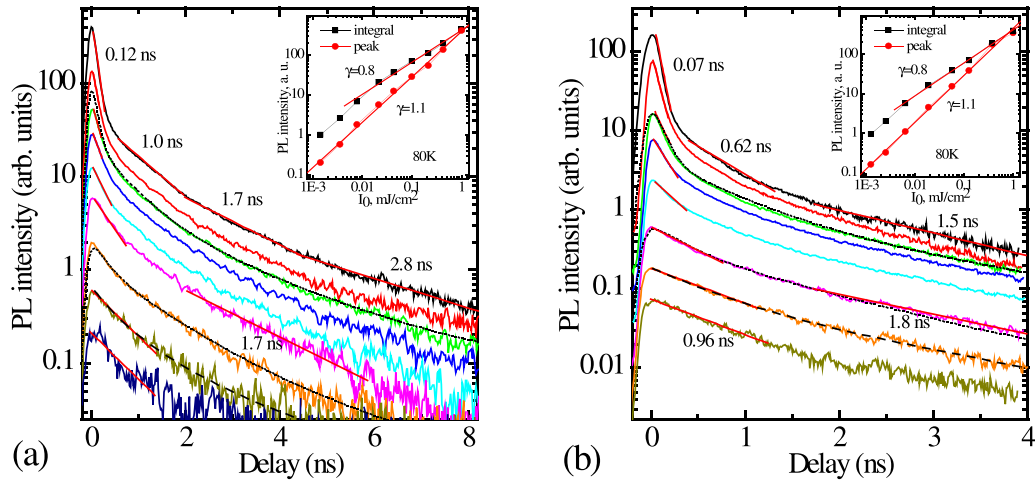


FIG. 2. Spectrally integrated PL band-edge decay transients in $\text{Al}_{0.61}\text{Ga}_{0.39}\text{N}/\text{Al}_{0.70}\text{Ga}_{0.3}\text{N}$ MQWs (a) and the $\text{Al}_{0.68}\text{Ga}_{0.62}\text{N}$ epilayer (b) at various excitation energy fluences I_0 and $T = 80$ K. The solid lines provide exponential decay fits, the dashed curves show two-exponential decay fits, while dotted curves represent modeled decays including two localizing centers (see Sec. III B). The insets show excitation dependencies of PL peak intensity values (circles) and of time-integrated PL intensity (squares) recorded at the same fluences as the decays.

to fluences of 2–20 mJ/cm^2 , which exceeds the range of excitation density we had access to.

At much lower energies than this band-edge emission near 5 eV, we observe the signatures of two PL bands related to defects. We call them “defect 1” at 330 nm (3.7 eV) and “defect 2” at 450 nm (2.75 eV). The first defect band is attributed to the PL signature of a vacancy-oxygen complex, while the second one is related to the PL signature of an aluminum vacancy [35,36]. The PL intensities of these defect-related PL bands quench with increasing temperature. It is notable that the PL intensity of band defect 1 is weaker in MQWs than in the AlGa_N layer, while the PL intensities of band defect 2 is rather similar in both samples. Thus, the similarities of the intensities of the band-edge emission for the MQWs and for the AlGa_N layer suggest that the vacancy (defect 2 PL band) can be responsible of the nonradiative quenching of the PL emission. The other one (defect 1 PL band) was also identified as an effective recombination center [37].

We first focus on the near band-edge emission in the 5-eV range. In Fig. 2 are reported the band-edge PL decay transients for the $\text{Al}_{0.61}\text{Ga}_{0.39}\text{N}/\text{Al}_{0.70}\text{Ga}_{0.3}\text{N}$ MQWs [Fig. 2(a)] and for the AlGa_N layer [Fig. 2(b)] within the very wide photoexcitation densities at a fixed 80-K temperature. The PL transients are confirming up to 550 K, the previously observed nonexponential PL decay in the MQWs at $T < 150$ K [19]. At low excitations and at short delays after the excitation pulse the PL transients are fitted, using an exponential function (the decay time $\tau_{\text{PL}} \approx 0.9$ ns corresponds to the time after the excitation pulse when the PL intensity is divided by e) and the addition of several complementary (and slower decays) are needed to account for the recombination kinetics in the PL tails (we choose here to use the times at long delays after the excitation pulse when the initial PL intensity is divided by e^2 and e^4). This analysis of the PL decay tails provided the lifetime values $\tau(80\text{ K}) = 1.5\text{--}2.8$ ns, being the lower limit of radiative lifetime. The determined by numerical calculations radiative lifetime is only slightly larger in these

tails ($\tau_{\text{rad}} = 2$ to 4 ns), when nonradiative recombination impact τ_{nr} is taken into account by the relation $1/\tau = 1/\tau_{\text{rad}} + 1/\tau_{\text{nr}}$ (see text further in this paper). The longer values of τ_{rad} in the tails reveal the entangled contributions of the spatial variation of localization potential in the layer, and/or of different separation of wave functions of electrons and hole by the polarization fields due to variations of the thickness of the quantum wells (variations of the contribution of the quantum confined Stark effect) [38]. When scaling the photoexcitation density from the low density conditions to the high density ones, one always records similar nonexponential shapes, with significant differences in the range of the highest densities, in a straightforward relationship with faster nonradiative and free-carrier radiative recombination processes.

In Figs. 3(a) and 3(b) are reported the decay times recorded for defect 1 330 nm at two temperatures (80 and 150 K) under different photoexcitation densities. Figures 3(c) and 3(d) are the analogs of Figs. 3(a) and 3(b) but at different temperatures (here 80 and 200 K) for the MQWs sample and they concern emission at 450 nm (defect 2). As alluded to it earlier, it is known that the first emission band is due to the transitions from a Si shallow donor to $V_{\text{III}}\text{-}3\text{O}_{\text{N}}$ (V_{III} are Ga and Al vacancies) while the second deeper one is due to electron to V_{Al}^{2-} vacancy transitions [35,39]. It is observed that the band at 330 nm (defect 1) exhibits a slow rise with excitation, which is due to the slow trap filling in the alloy. This rising becomes slower with increasing temperature. The 450-nm band exhibits a decay similar to that of excitons/carriers reported in Figs. 2(a) and 2(b), indicating that, in the MQWs, the trap should be an efficient nonradiative recombination center, as determined by positron annihilation spectroscopy [37]. The decay time of the emission labeled defect 2, reflecting the nonradiative recombination rate, is larger at highest excitations and lowest temperatures due to the fast radiative recombination rate of free carriers. The recombination of a hole to an aluminum vacancy V_{Al}^{3-} is much faster than the recombination of an electron to an aluminum vacancy V_{Al}^{2-} and it is thus hardly observed here, due to our limited temporal resolution. Thus

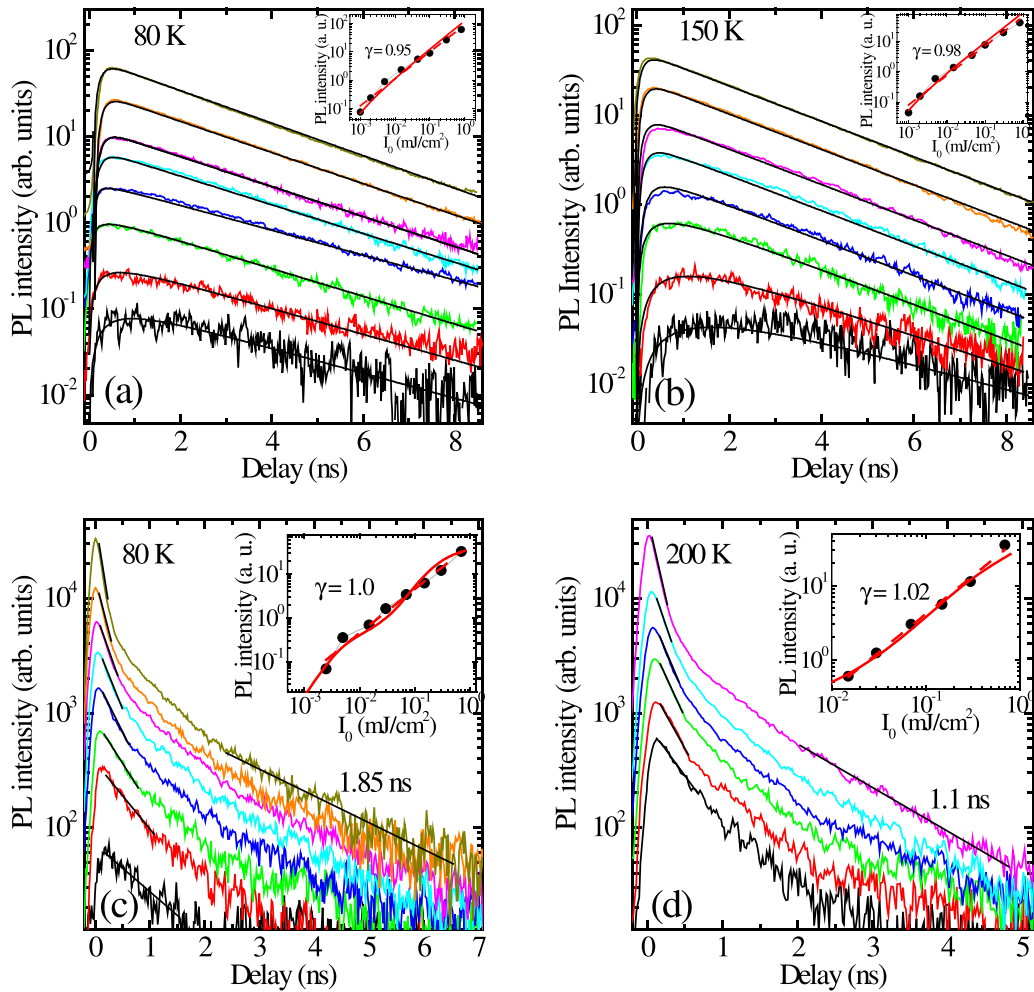


FIG. 3. Evolution of the spectrally integrated PL defect decay transients recorded under different photoexcitation densities at different temperatures (80 and 150 K) for the 330-nm band in the case of the $\text{Al}_{0.68}\text{Ga}_{0.62}\text{N}$ epilayer (a) and (b) and their analogs (now at 80 and 200 K) for the 450-nm band in the case of the $\text{Al}_{0.61}\text{Ga}_{0.39}\text{N}/\text{Al}_{0.70}\text{Ga}_{0.3}\text{N}$ MQWs (c) and (d). The insets show the dependencies of the PL peak intensity against excitation density (circles). Dashed lines in the insets show linear fits in log-log scale, defined by γ slopes, while solid lines show fits according to Eqs. (18) and (22).

the defect 2 band does not exhibit considerable rise time as in the case of the $V_{\text{III}}\text{-}30_{\text{N}}$ trap. The kinetics of the PL peak intensities for defect 2 also follow a linear dependence against excitation density, which indicates that emission from this defect band is of an electron-acceptor nature, as in the range of high excitations, traps (which density is much smaller than excited electron-hole pair density) are filled with holes.

In Fig. 4(a) are displayed the Arrhenius plots of the temperature dependences of the near band-edge PL for the AlGa_N layer (squares) for the MQWs (circles), for defect 1 at 330 nm (triangles) and for defect 2 (diamonds). Obviously defect 2 departs from the general trend. The temperature dependences of the decay times in the initial parts (short delays after the excitation pulse) and in the tail parts (long delays after the excitation pulse) are very similar, but they differ by a factor of about 2 [see Fig. 4(b)]. A two-exponential fitting of decay curves at low excitations and different temperatures provides rather similar amplitudes for the fast and for the slow components at low temperatures, while at high temperatures the slow component amplitude becomes few times lower than that of fast one. These facts indicate that the origin of the

nonexponential decay is plausibly correlated to the existence of nonhomogeneously distributed random localizing potentials. In the following we will restrict our analysis to the short delay part, that is to say from now to decay time $\tau_{1\text{PL}}$ as they represent the most well defined electron-hole pair density.

Let us consider the MQWs sample. When the excess carrier densities reach values of $\Delta N_0 \sim 1\text{--}2 \times 10^{18} \text{ cm}^{-3}$, the values of $\tau_{1\text{PL}}$ start to decrease with increasing excitation density, and this produces transients up to an order of magnitude faster than at low excitation density [~ 120 ps; see Fig. 2(a)]. Very similar excitation-enhanced decay was also observed in the $\text{Al}_{0.68}\text{Ga}_{0.62}\text{N}$ epilayer, reaching at the highest excitation density the lower value of 70 ps [see Fig. 2(b)]. In both samples, the decrease of the lifetime measured at 80 K followed a power dependence $\tau_{1\text{PL}} \propto I_0^{-0.4}$. We emphasize that this joint measurement of similar nonexponential PL decay and of a fast transient decreasing with the excitation density is observed at 300 K as well. The low-temperature time-integrated PL intensity I_{TIPL} increases linearly up to $\Delta N_0 \approx 10^{18} \text{ cm}^{-3}$, and starts to exhibit a gradual saturation in the range of higher densities of excitation (see insets in Fig. 2, where the slope value

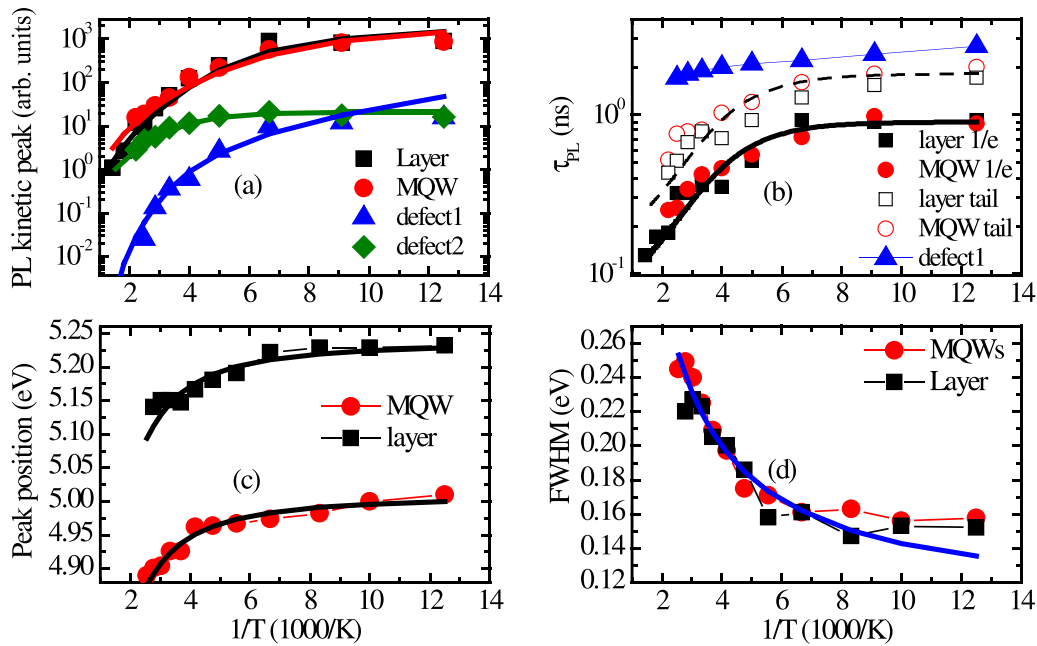


FIG. 4. (a) Arrhenius plots of the TRPL peak intensity for the AlGaIn epilayer, MQWs structure, and defects. (b) Arrhenius plots of the PL decay times in the short delay range ($1/e$ drop) and in the long delay range (tail, $1/e^2$ to $1/e^4$ drop). The 10^{18} cm^{-3} excitation was used to determine the latter parameters. The dashed curve is obtained by multiplying the solid fitting curve by a factor of 2. (c) Temperature dependences of free exciton PL peak positions. (d) Arrhenius plots of the FWHM of the PL band-edge peaks. Solid lines represent fits according to Varshni's equation and in terms of the thermal broadening.

γ of the excitation dependence, $\log(I_{\text{TIPL}})$ vs $\log(I_0)$ changes from $\gamma = 1.0$ to 0.8). On the other hand, the value of the intensity of the peak PL I_{PL0} (at $t = 0$) increased linearly with excitation, and the slope of its dependence against excitation density remains nearly linear in the whole range of excitation [$I_{\text{PL}}(t = 0) \propto I_0^{1.1}$; see circles in the inset of the Fig. 2]. The value of $\gamma_{\text{PL}} \approx 1.0$ points out that the radiative lifetime (τ_{Rad}) in both samples is almost excitation independent (this can be deduced from the dependence of the radiative recombination rate against excitation as $I_{\text{PL}}(t = 0) \sim \Delta N_0 / \tau_{\text{Rad}}$, which is valid here, as $\tau_{\text{1PL}} > \tau_L$). This permits us to safely attribute the change of the TIPL slope (observed from 1.0 to 0.8) to the increase of the nonradiative recombination rate.

We now have a backward look to Figs. 4(a)–4(d) where we plot the evolutions of the PL peak intensities, of the PL decay times, of the energies of the PL emission peaks, and the variations of the FWHM on temperature. These figures teach us that the exciton dissociations in wells and layers are rather similar: band defect 1 activates much faster than band defect 2, due to a weaker defect capture cross section and Si donor ionization. The PL peaks all redshift on temperature in all bands due to the reduction of band gap with temperature and the broadenings also increase, due to interaction with phonons. The band edge emission peak is much larger than kT , and this is an evidence of the existence of a strong inhomogeneous disorder in the material, making the track of the excitation dependencies difficult.

The temperature dependencies of band-edge peak positions were fitted using Varshni's empirical equation $E(T) = E(0) - aT^2/(b + T)$ [40] with $a = 1.2 \times 10^{-3} \text{ eV/K}$, $b = 1000 \text{ K}$, and $E(0) = 5.007 \text{ eV}$ for MQWs; and $a = 1.3 \times 10^{-3} \text{ eV/K}$, $b = 1000 \text{ K}$, $E(0) = 5.236 \text{ eV}$ for the AlGaIn

layer, respectively. The very slight differences in the values of the fitting parameter a and b are correlated to the similar compositions of both structures. In comparison, similar values of $a = (1.0\text{--}1.2) \times 10^{-3} \text{ eV/K}$, $b = 1100 \text{ K}$ for $x = 0.56$ AlGaIn are available in the literature [41]. The broadening of the PL band at low temperature is due to the cross talking between the excitonic emission at high energy and the contribution of localized excitons (12–35 meV localization energy) at lower energy.

Complementary TRPL measurements were also performed at higher temperatures, up to 550 K. The PL peak intensity decreases from I_{PL0} down to three orders of magnitude in the 80–550-K range in both samples, whatever the photoexcitation density is. This leads to the decrease of PL efficiency reported in Figs. 5(a) and 5(b). This decrease is due to dissociation of excitons and to the reduction of the bimolecular recombination rate. However, we remind the reader that the decrease of the PL lifetime observed when increasing the temperature is some orders of magnitude smaller [see Figs. 4(a) and 4(b)], which is due to the enhancement of nonradiative recombination rate with increasing temperature. The temperature dependence of $I_{\text{PL0}}(T)$ was fitted using Eq. (4): [42].

$$I_{\text{PL0}}(T) = \text{PL}_0 / [1 + A \times \exp(-E_0/k_B T)]. \quad (4)$$

Here, E_a corresponds to thermal dissociation energy of excitons, PL_0 is the low-temperature PL amplitude. The values we obtain for E_a are 145 and 103 meV for the AlGaIn layer and MQWs, respectively. Values of constant A are 8000 and 1000 for the AlGaIn layer and MQWs, respectively. We obtain a lower activation energy of excitons in the MQWs compared to the value we get for the AlGaIn layer. As an explanation of this, we invoke lower modulations of the composition x in

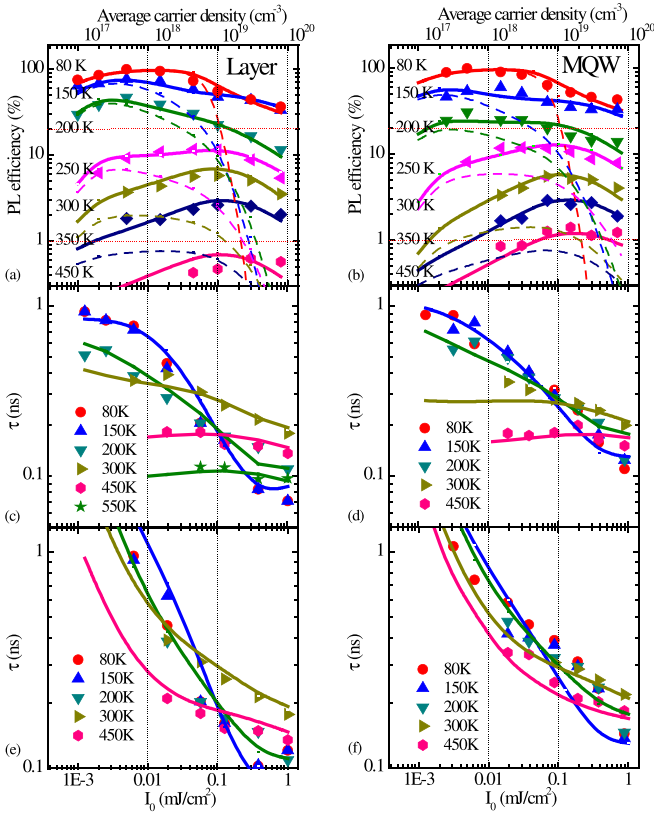


FIG. 5. Excitation dependencies of TIPL efficiency η_{PL} (a) and (b), band-gap PL decay time (c) and (d), and decay time of the emission of vacancy defect 2 (e) and (f), at various temperatures in the $\text{Al}_{0.68}\text{Ga}_{0.32}\text{N}$ layer and MQW, respectively. Dashed lines in (a) and (b) show the contributions of excitons to PL efficiency, while solid lines include both excitons and carriers.

MQWs and their corresponding impact on the energy levels of the quantum wells.

Figure 5 is organized over a coherent ensemble of six windows. From Figs. 5(a) to 5(f) we report, at temperatures ranging from 80 K to 550 K, the following:

(i) the evolutions of the TIPL efficiency η_{PL} against the excitation density for the AlGaIn layer and for the MQWs, respectively [Figs. 5(a) and 5(b)];

(ii) the evolution of the PL decay times at the band gap (time after the excitation pulse when the intensity of the TIPL is diminished by a factor e) for the AlGaIn layer and for the MQWs, respectively [Figs. 5(c) and 5(d)];

(iii) the decay time of emission at the energy of the defect 2 for the AlGaIn layer and for the MQWs, respectively [Figs. 5(e) and 5(f)].

The PL efficiency exhibits the largest value at the lowest temperature and for medium excess carrier densities. The trends recorded for the decay times of the PL at the band-gap energies are very similar in the AlGaIn layer and MQWs, indicating similar recombination mechanisms. The reduction of lifetime with excitation is more pronounced at low temperatures compared to its reduction at high temperature, in relationship with stronger radiative recombination processes. In the 80–200-K range, we observe a slight increase of η_{PL} with excitation up to reaching a peak value at excess carrier density $\Delta N_0 \approx 10^{18} \text{ cm}^{-3}$, which is attributed to a competition between the exciton radiative recombination and the saturation of the traps [27]. Further increase of the excitation energy density leads to provoke a gradual decrease of η_{PL} as a straightforward consequence of the decrease of the nonradiative lifetime. At $T > 200 \text{ K}$, the value of η_{PL} at low excitation decreases, as a proof of the increasing impact of the thermal dissociation of excitons and of a more efficient capture of delocalized carriers by nonradiative recombination centers. At higher temperatures, the free-carrier nonradiative recombination processes dominate. They are weakly excitation dependent. The lifetime slightly reduces with temperature due to the increasing thermal speed of free carriers. The lifetime of the defect 2 band has very similar decay time at high excitation due to the fast hole capture by aluminum vacancies and it follows the electron density.

At this stage, it is obvious that a detailed understanding requires a full modeling of the carrier-exciton formation and of the recombination processes. This we are handling in the next section.

B. Modeling of the exciton-carrier transport

A global numerical modeling including the relevant and power-dependent quantities for the analysis that are density of free excitons Δn_{fex} , the density of localized excitons Δn_{llex} , and the free-carrier densities Δn_{fc} as well as their corresponding recombination and emission mechanisms has been conceived and its solutions have been computed. The PL intensity (PLI) was fitted with Eq. (5), derived according to Refs. [43,44]. The latter includes the radiative emission of both free carriers PLI_{fc} , free excitons PLI_{fex} , and localized excitons PLI_{llex} .

$$\begin{aligned} \text{PLI}(\Delta N) &= \text{PLI}_{\text{fc}}(\Delta n_{\text{fc}}) + \text{PLI}_{\text{fex}}(\Delta n_{\text{fex}}) + \text{PLI}_{\text{llex}}(\Delta n_{\text{llex}}) \sim B f_h \Delta n_{\text{fc}} (f_e \Delta n_{\text{fc}} + n_0) + \Delta n_{\text{fex}} / \tau_{\text{fex}} (\Delta n_{\text{fc}}) + \Delta n_{\text{llex}} / \tau_{\text{llex}} (\Delta n_{\text{fc}}), \\ \Delta N &= \Delta n_{\text{fc}} + \Delta n_{\text{fex}} + \Delta n_{\text{llex}}, \quad \Delta n_{\text{fex}} = \Delta n_{\text{fc}} f_h (f_e \Delta n_{\text{fc}} + n_0) / n^*. \end{aligned} \quad (5)$$

Equation (5) contains a lot of parameters depending on the alloy compositions and on the design of the MQWs sample. In the equation above, the hole and the electron density in the wells are described by relations $\Delta n_h = f_h \Delta n_{\text{fc}}$ and $\Delta n_e = f_e \Delta n_{\text{fc}}$ respectively, where f_e and f_h represent the well occu-

pation factors in the case of electrons and holes. B represents the excitation-dependent bimolecular radiative recombination coefficient. The conservation law requires that the density of free carriers augmented by the density of excitons is equal to the density of generated electron-hole pairs ΔN .

The exciton and free-carrier relation holds with an exciton formation factor [43]:

$$n^* = N_{\text{dosfex}} = \exp(-E_{\text{fex}}(\Delta n_{\text{fc}})/k_B T), \quad (6)$$

where N_{dosfex} is the excitonic density of states, E_{fex} , which represents the free exciton thermal ionization energy [44]:

$$E_{\text{fex}}(\Delta n_{\text{fc}}) = E_{\text{fex0}}(1 - [\Delta n_{\text{fc}}/N_{\text{crit}}]^{1/3}). \quad (7)$$

Here N_{crit} is the critical Mott density. It is correlated with the Bohr radius a_B as follows: $a_B N_{\text{crit}}^{1/3} = 0.25$; E_{fex0} is the exciton dissociation energy at low excitation:

$$E_{\text{fex0}} = \hbar^2(2\mu a_B^2)^{-1}, \quad (8)$$

E_{fex0} is related to a_B and to the exciton reduced mass $\mu = 0.26 m_0$ where it is obtained by the equation $1/\mu = 1/m_e + 1/m_h$ in terms of the electron (respectively hole) effective mass m_e (respectively m_h).

In AlGaN alloys with $x = 0.7$, $m_e = 0.28 m_0$ [45,46], $m_h = 4m_0$ (the latter value was interpolated between $m_h = 1.4 m_0$ in GaN and $m_h = 5m_0$ in AlN [47]). The latter values of masses lead to a three-dimensional (3D) electron density of states of $4 \times 10^{18} \text{ cm}^{-3}$ and to a 3D hole density of states of $3 \times 10^{20} \text{ cm}^{-3}$. This is indicating that holes are not degenerated and weakly activated from the wells in our experiments.

In terms of the well thickness d_W , the volume effective density of states (describing the statistics) for electrons and holes are: $N_{We} = m_e/\pi \hbar^2 kT/d_W = 4.3 \times 10^{19}$ and $2.2 \times 10^{19} \text{ cm}^{-3}$ and $N_{Wh} = m_h/\pi \hbar^2 kT/d_W = 6 \times 10^{20}$ and $3 \times 10^{20} \text{ cm}^{-3}$, respectively. The first value here and further below is for the AlGaN layer ($d_W = 0.7 \text{ nm}$), while the second is for the MQW ($d_W = 2 \text{ nm}$). Holes thus are not degenerate in our experiments. For excitons the density of states is $N_{\text{dosfex}} = \mu/\pi \hbar^2 kT/d_W = 4 \times 10^{19}$, and $2 \times 10^{19} \text{ cm}^{-3}$ at RT. The densities of states in the wells are $m_{e,h}/\pi \hbar^2 \Delta_{e,h}/d_W$ ($\Delta_{e,h}$ are the electron or the hole energy levels measured with respect to the bottom of the well), which gives $1.0 \times 10^{21} \text{ cm}^{-3}$, $1.3 \times 10^{20} \text{ cm}^{-3}$ for electrons and $1.4 \times 10^{21} \text{ cm}^{-3}$, 6.4×10^{20} for holes. Thus, under our experimental conditions, the wells are not overfilled with carriers.

The 3D exciton binding energy $E_{\text{ex0}} = 13.6 \text{ eV} \mu/\varepsilon^2 = 46 \text{ meV}$ in $x = 0.7$ AlGaN is calculated using dielectric constant $\varepsilon = 8.8$. The value of the 3D exciton Bohr radius is then $a_{B0} = 1.9 \text{ nm}$ [41]. Using the relative exciton binding energy $E_{\text{ex}}/E_{\text{ex0}}$ dependence on the dimensionless well thickness d_W/a_{B0} [48] for our samples provides $E_{\text{ex}}/E_{\text{ex0}} = 2.2$ and 2.8 values, which render $E_{\text{ex}} = 101$ and 129 meV in the MQWs and in the layer, respectively, being well consistent with the experiment (104 and 140 meV). The values of the Bohr radii in the wells and SSL layer then are 1.3 and 1.1 nm as calculated by relation $E_{\text{ex}} = \hbar^2(2\mu a_B^2)^{-1}$. Critical exciton densities then are calculated by using Mott criterion, $a_B N_{\text{crit}}^{1/3} = 0.25 : 0.7 \times 10^{19} \text{ cm}^{-3}$ in MQWs and $1.1 \times 10^{19} \text{ cm}^{-3}$ in the AlGaN layer.

In AlGaN-based heterostructures conduction-band offset is taken as being a 70% distribution of the total band offset between the two nitride compounds used to grow the well material and the barrier material. The values of the total values band offsets $\Delta E_g = 0.8$ and 0.3 eV were calculated in the layer and MQWs, respectively. They represent the band

offsets between $\text{Al}_x\text{Ga}_{1-x}\text{N}$ and $\text{Al}_y\text{Ga}_{1-y}\text{N}$ in cases $x - y = 0.32$ and $x - y = 0.09$, respectively.

For a narrow QW of thickness d_W , of depth ΔE , the position of the first energy level E_1 , measured relatively to the bottom of the well is for a particle of mass m

$$\delta = \sqrt{2m\Delta E_C}d_W/\pi \hbar \ll 1; \quad E_1 = \frac{-\pi^2}{4}\delta^2 \Delta E. \quad (9)$$

The condition is satisfied by $\delta = 0.55$ and 0.54 in the MQWs and the SSL layer. Electron energy levels are $\Delta_e = 0.16$ and 0.57 eV below the position that would have the conduction band in bulk barrier layers. Δ_e levels are very deep thus thermal activation will not be impacting, but for the shallower hole level, activation would be possible. For holes that the ultranarrow well condition is not satisfied and the energy level above the bottom of the well can be framed by the standard relation for the infinite well potential

$$E_1 = \frac{-\pi^2 \hbar^2}{2m_h d_W^2}. \quad (10)$$

The calculations render energy levels Δ_h of 42 meV in MQW and 48 meV in the layer above barrier energy. The values observed for the experimental activation energy ($43 \pm 20 \text{ meV}$) well coincide with them. Holes and excitons are thus localized in the wells.

The calculation of the transition energy between the levels of electron and hole levels provides energies of 4.9 eV in the AlGaN layer and 5.0 eV in the MQWs corresponding to values of emission wavelengths at 248 and 253 nm that are very similar to the experimental ones (242 and 252 nm).

The shift of PL with excitation power is weak (the emission appears near the bottom of the QW for electron), and the free-carrier emission saturates at high excitation densities. In the range of low density of excitations the excitonic emission prevails, but with the increase of excitation, due to band-gap renormalization (BGR) the Mott transition occurs [49] (in GaN the BGR is $4.3 \times 10^{-8} \text{ eV} \times \Delta N^{1/3} = 80 \text{ meV}$ at $\Delta N = 10^{19} \text{ cm}^{-3}$) and the PL peak position appears very weakly excitation dependent. This is really tricky to measure: the large broadening of the peak complicates the observation of shifts versus excitation and is also a correlation between the temperature and the variations of the PL emission peak in connection with the reduction of the band gap with temperature.

We have taken into account the evolution of the oscillator strength for the electron-hole transitions versus temperature. Here we model it using the normalized temperature-dependent oscillator strength [50]:

$$f_{\text{osc}} = \exp[-\langle S \rangle \coth(\langle \hbar\omega \rangle/2k_B T)], \quad (11)$$

where $\langle \hbar\omega \rangle$ and $\langle S \rangle$ are the averaged optical-phonon energy (involved in optical transitions) and the exciton-phonon interaction strength, respectively. An average phonon energy of 95 meV was used [51] and the value of the exciton-phonon interaction factor $\langle S \rangle = 0.5$ was used [52]. This gives substantial variations of the oscillator strength that is reduced from 0.96 at RT down to 0.52 at 550 K. Due to small well thickness, the quantum confined Stark effect and its screening with carrier density were neglected for simplicity.

Assuming that the exciton formation is much faster than its recombination, the time-dependent variation of the density of

excited electron-hole pairs can be described by equation [43]

$$d\Delta N/dt = G - \Delta n_h/\tau_{nr} - \Delta n_{fex}/\tau_{fex}(\Delta n_{fc}) - \Delta n_{lex}/\tau_{lex} - Bf_h\Delta n_{fc}(\Delta n_{fc} + n_0) = G - \Delta N/\tau. \quad (12)$$

Equation (12) eliminates the dynamic balance between the free carriers and the excitons and it provides a straightforward determination of the recombination parameters: the effective carrier lifetime τ (determined from PL decays) and of the nonradiative lifetime of vacancies τ_{nr} . Here Δn_h , Δn_{fex} , Δn_{lex} , Δn_{fc} are the concentrations of holes, free excitons, localized excitons, and free carriers, respectively. Here, τ_{fex} and τ_{lex} represent the radiative lifetimes of the free and of the localized excitons, respectively. G is the generation function [28]. The balance between free and localized excitons is described by equation

$$d\Delta n_{lex}/dt = c_{lf}\Delta n_{fex}(N_{loc} - \Delta n_{lex}) - c_{lf}\Delta n_{lex}N_{dosx} \exp(-E_{loc}/kT). \quad (13)$$

Here E_{loc} is the exciton localization energy, N_{loc} is the density of localized states, c_{lf} are rate coefficients. Assuming the dynamic equilibrium $d\Delta n_{lex}/dt = 0$, the latter rate equation provides the ratio of localized excitons to free exciton density:

$$\begin{aligned} \Delta n_{lex}/\Delta n_{fex} &= (N_R - \sqrt{N_R^2 - 4\Delta n_{fex}N_{loc}})/2 \\ &\approx 1/[1 + \Delta n_{fex}/N_{loc} \\ &\quad + N_{dosx} \exp(-E_{loc}/kT)/N_{loc}]; \\ N_R &= \Delta n_{fex} + N_{loc} + N_{dosx} \exp(-E_{loc}/kT). \end{aligned} \quad (14)$$

The excitation dependent bimolecular radiative recombination coefficient is described by relation $B = B_{rad0}/(1 + \Delta n_{fc}/2N_{cd})$ [53,54]. Here B_{rad0} is the nondegenerate bimolecular recombination coefficient and N_{cd} is the density of states in the conduction band. The relation is valid when the density of states in the valence band, N_{vd} , is much larger than the density of states in the conduction band, N_{cd} [53].

The internal quantum efficiency IQE is calculated using the ratio of the radiative to the total recombination rate as

$$IQE = \frac{\Delta n_{fex}/\tau_{fex}(\Delta n_{fc}) + \Delta n_{lex}/\tau_{lex} + Bf_h\Delta n_{fc}(\Delta n_{fc} + n_0)}{\Delta n_{fc}/\tau_{nr} + \Delta n_{fex}/\tau_{fex}(\Delta n_{fc}) + \Delta n_{lex}/\tau_{lex} + Bf_h\Delta n_{fc}(\Delta n_{fc} + n_0)}. \quad (15)$$

The tedious fittings of the PL efficiency and of the lifetimes against density of excitation and for different temperatures (Fig. 5) based on the resolutions of Eqs. (12)–(15) leads us to the following values of the recombination parameters:

$$\begin{aligned} B_{rad0} &= f_{osc} \times (7 \pm 1) \times 10^{-10} \times (T/300)^{-3/2} \text{ cm}^3/\text{s}, \\ 1/\tau_{fex} &= f_{osc} \times (0.6 \pm 0.2) \times 10^9 \times (T/300)^{-1} \text{ 1/s}, \\ E_a &= 104, 140 \pm 10 \text{ meV}, \\ f_h &= [2 + pT^2 \exp(-E_{ah}/k_B T)]^{-1}, \\ p &= (2 \pm 1) \times 10^{-4} \text{ K}^{-2}, \\ E_{ah} &= (43 + 20) \text{ meV}, \\ \tau_{nr} &= [\tau_h(n_0 + \Delta n_{fc}) + \tau_e \Delta n_{fc}]/(n_0 + \Delta n_{fc}), \\ \tau_e &= (160 \pm 30) \times (T/300)^{-0.5} \text{ ps}, \\ \tau_h &= (40 \pm 10) \times (T/300)^{-0.5} \text{ ps}. \end{aligned} \quad (16)$$

Here f_h is the hole occupation factor in QWs. The fitted values of the electron (τ_e) and hole (τ_h) lifetimes were obtained using the lifetime of recombination on traps τ_{nr} [55]. This latter lifetime is described at high excitations by the bipolar lifetime of carriers $\tau_{nr} = \tau_h + \tau_e$.

The initial decay was selected for the determination of the lifetime as it corresponds to an average decay rate over differently localized excitons and carriers at fixed excitation density. The value of the exciton radiative lifetime that we determine at RT is 1.7 ns. It is similar to what was published for GaN-AlGAN QWs: 0.8–1.4 ns [56]. Note that for the nonradiative recombination of hole on vacancies (and dislocations) the activation of hole is not considered as vacancies are located in both the barrier layers and in the well layers. More-

over, the values obtained for the capture cross sections ($\sigma = \pi d_c^2/4$) obtained by using the Shockley Reed Hall (SRH) lifetime model [57] and Eq. (16) are $\sigma_e = 1.5 \times 10^{-13}$ and $\sigma_h = 7 \times 10^{-13} \text{ cm}^2$ for electrons and holes respectively. With these values we calculate defect diameters for capture of $d_c = 4$ and 8 nm for electrons and holes respectively. Knowing the value of the trap density: $5 \times 10^{15} \text{ cm}^{-3}$, we calculate that the mean distance between traps is ~ 60 nm, a value larger than the capture diameters d_c . Thus, localized excitons (holes) will need activation from nm-sized localizing states [58] and they will then move along the QWs to the defects. At low temperatures, they will recombine more slowly than at high ones.

The radiative lifetimes are insensitive to the details of the quantum localizing potential (departure from perfection due to local variations of the well widths or variations of the alloy compositions) forming some kind of quantum dots with inhomogeneously varying shapes and compositions, but they strongly depend on the charge separation factor (quantum confined Stark effect) similarly to what was found in InGaN/GaN quantum dots [58]. The observed nonexponential decay (Fig. 2) arises from complex and broad distribution of lifetime, and not from a dynamical screening. The variations of lifetime are dominantly due to built-in electric fields.

For the verification of the determined set of parameters (16) we performed numerical calculations of the PL decays at few excitation fluences (Fig. 2) using Eqs. (12)–(14) and the carrier generation function $G = \alpha I_0 (\pi^{1/2} h\nu)^{-1} \exp(-4t^2/\tau_L^2)$ [28] with $\tau_L = 20$ ps in Eq. (12). The modeled curves at 80 K rather well describe the experimental decays with a distribution of localization energy E_{loc} . Fitting of the decay provided densities of two localizing centers by solving a set of two equations (14), where two localized exciton

energy values of $E_{\text{loc}1} = 12$ meV and $E_{\text{loc}2} = 35$ meV with densities $N_{\text{loc}1} = 5 \times 10^{18}$ cm $^{-3}$ and $N_{\text{loc}2} = 3 \times 10^{18}$ cm $^{-3}$, respectively, were used. We note that these two localization energies correspond to the fast and slow PL decay components with lifetimes of $\tau_{\text{lex}1} = 2$ ns and $\tau_{\text{lex}2} = 4$ ns. The longest decays correspond to more separated electron holes and to deeper localization potentials. In comparison, we refer to Ref. [59] where similar localization energy of around 20 meV for excitons with ~ 150 meV dissociation energy was observed in GaN/AlGaIn QWs [59]. Excitons, localized on QDs, have almost temperature-independent lifetime, thus the almost constant radiative lifetime at low temperature is due to the dominance of localized excitons [60,61]. According to Ref. [58], using Eq. (17),

$$\tau_{\text{lex}} = \varepsilon_0 m_0 c_0^3 h^2 / (2\pi n e^2 E_{\text{lex}}^2 \phi_{\text{eff}}) \quad (17)$$

(here E_{lex} is the emission energy of the localized exciton, n is the refractive index at E_{lex}) we obtain $\tau_{\text{lex}} = 0.5$ ns if excitons are not subject to electric fields (electron-hole wave-function overlap is $\phi_{\text{eff}} = 1$). According to Ref. [62] $\phi_{\text{eff}} = 0.37$ in a 1.5-nm-thin QW with $x = 0.6$ AlGaIn QWs and AlN barriers. Under these conditions the lifetime of localized exciton is increased to 1.4 ns, a value that pleads in favor of more weakly localized excitons, with a lifetime of 2 ns in our experiments. We determine the free exciton lifetime to increase linearly with temperature $\tau_{\text{fex}} \sim T$ [56] with 7 ps/K slope coefficient. This coefficient is comparable to values reported for GaN/AlGaIn QWs, 11 ps/K, and ZnO/MgZnO QWs, 7 ps/K [60].

The exciton localization energies are rather small in comparison to the widths of the PL spectra. Thus in the TRPL decay, a spectral shift of 15 ± 5 meV is observed with time passing. It is also noticeable to remark that quantum yield remains unchanged at long delays, indicating that both radiative and nonradiative processes are then deactivated.

Thanks to the phenomenon of charge separation, holes are localized in small volume region, and experience potential E_{loc} barriers for nonradiative recombination. The localized exciton fractions are $n_{\text{lex}}/n_{\text{fex}} = 0.19$ ($E_{\text{loc}1} = 12$ meV) and 0.31 ($E_{\text{loc}2} = 35$ meV) at 300 K and 10^{18} cm $^{-3}$ excitation, confirming the existence of fast-decay and slow-decay components even at room temperature.

C. Modeling of the defect-related emission

The PL intensity related to the aluminum vacancy-oxygen complex defect (defect 1) is described by the relation

$$\text{PL}_1(\Delta N) = N_{\text{Si}^0}(\Delta N) N_{T1}(\Delta N) f_h, \quad (18)$$

which well describes the almost linear dependencies of peak PL intensity observed and drawn in Figs. 3(a) and 3(b). This recombination process consists of donor acceptor pair (DAP) transitions involving a neutralized Si donor [with N_{Si^0} concentration in Eq. (18)] to neutralized acceptor [with N_{T1} concentration in Eq. (18)]. The increase of the PL intensity with excitation is due to the faster filling of acceptors with holes and donors with electrons under increasing carrier concentration. Against excitation the donor filling is described by the relation [63]

$$N_{\text{Si}^0}(\Delta N) = N_{\text{Si}} [1 + N_C / 2(n_0 + \Delta N)]^{-1}. \quad (19)$$

Here N_{Si} is total Si donor concentration with an activation energy of 30 meV [64] and n_0 is the equilibrium electron density. The change of the filled trap density N_{T1} by progressive filling satisfying the condition $n_T < \Delta N$, where n_T is the total trap density, can be described by the following differential equation:

$$dN_{T1}/dt = \sigma v_{\text{th}} \Delta N (n_T - \Delta N) \quad (20)$$

with σ the capture cross section and v_{th} the thermal velocity of excitons (holes). A solution of Eq. (20) is given by relation

$$N_{T1}(t) = \frac{n_T \{\exp(\sigma v_{\text{th}} n_T t) - 1\} \exp(-t/\tau_{\text{DAP}})}{\exp(\sigma v_{\text{th}} n_T t) - (\Delta N - n_T)/\Delta N}. \quad (21)$$

The calculation of the values of the absolute cross sections σ requires the knowledge of the thermal velocity $v_{\text{th}} = (8kT/\pi m_t)^{0.5}$. Here $m_t = m_e + m_h$ is the exciton translational mass of $4.3m_0$ (similar to holes); it provides the following value of the thermal velocity $v_{\text{th}} = 5 \times 10^6$ cm/s. At excitation densities higher than the trap density, after stabilization, the ratio of the trapped exciton density relatively to the total excited density is $r = (1 - n_{\text{traps}}/\Delta N_0)$ where n_{traps} is the trapped carrier density.

This factor describes the drop of QE at low excitation and from the fit [see drop of η_{PL} in Fig. 5(a) at $\Delta N \sim \Delta n_{\text{ex}} < 3 \times 10^{17}$ cm $^{-3}$] in the AlGaIn layer the value $n_T = 0.5 \times 10^{17}$ cm $^{-3}$ is obtained. Further using that value, and fitting with the help of Eq. (21) the trap filling curves in Figs. 3(a) and 3(b), we obtain the value of the trap capture cross section of $\sigma = (2 \pm 1) \times 10^{-16} \times (300/T)^2$ cm 2 from the relation $\tau = 1/\sigma v_{\text{th}} n_T$.

Excitons feel the defect potential (assumed to be long range and of Coulomb-type $V \sim 1/r$). The capture probability reduces with temperature as excitons have a large thermal velocity at high temperatures. Comparing the trap filling at 80 and 150 K, it evidences the strong reduction of the trapping cross section with temperature due to the Coulombic nature of the interactions. Excitons are neutral, thus their capture to the $V-30_N$ trap may be subject to a hole capture following their ionization near traps. The defect lifetime weakly changes with temperature, indicating that holes are accumulated onto this deep defect 1 and they further need a large thermal activation energy to be released to the valence band for much faster nonradiative recombination. The value of the lifetime of 2–3 ns plausibly originates from a radiative electron from the Si donor to the (acceptor) excited defect 1 transition. The defect lifetime slightly reduces with temperature plausibly due to the increase of the acceptor activation. The peak intensity of the defect emission varies with temperature similarly to the intensity of the excitonic peak [see Fig. 4(a)], as an evidence for weaker exciton capture and emission at higher temperatures. The evolution of the PL intensity of defect 1 band with temperature, $\text{PL}_1(T)$ was fitted as $\text{PL}_1(T) \sim f_h \times N_{\text{Si}^0}(\Delta N, T) / [1 + \sigma(T) v_{\text{th}} \Delta N / \tau_{\text{DAP}}(T)]$. The maximum of the kinetics peak was obtained when the derivative of Eq. (21) is equal to zero. The last factor accounts for a capture process becoming slower than a DAP recombination process with τ_{DAP} decay time [see Fig. 4(b)].

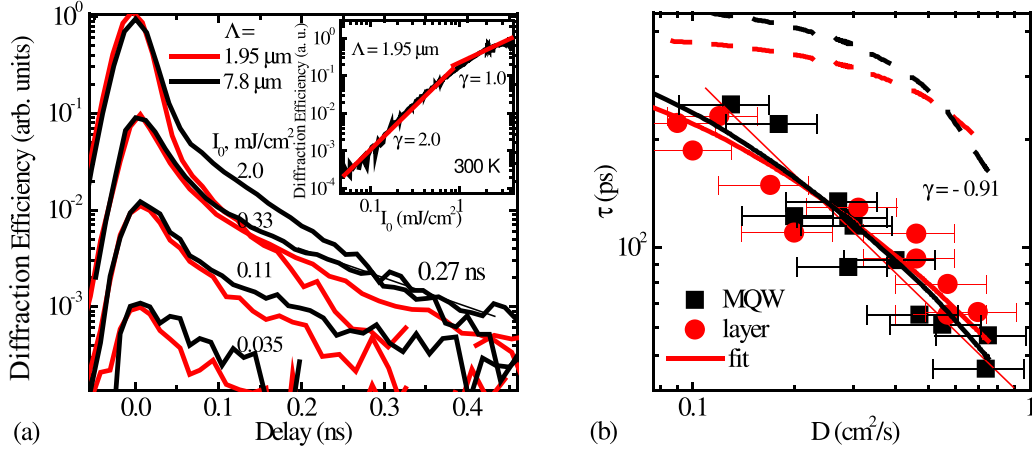


FIG. 6. (a) LITG decays at different grating periods and excitations. Inset is the plot of the diffraction efficiency against the excitation density. γ are the slopes of the curves in the log-log plot. (b) The correlation between the carrier lifetime and the diffusion coefficient in highly excited $\text{Al}_{0.61}\text{Ga}_{0.39}\text{N}/\text{Al}_{0.70}\text{Ga}_{0.3}\text{N}$ MQWs and $\text{Al}_{0.68}\text{Ga}_{0.62}\text{N}$ epilayer. Solid lines are a fit according to Eq. (24). Dashed lines show the impact of vacancies to the recombination lifetime.

The evolution of the intensity of the PL related with the aluminum vacancy (defect 2) was described as

$$\text{PL}_2 = (\Delta N + n_0)N_{T2}f_h; \quad (22)$$

N_{T2} is the trapped to the defect hole density. As the exciton and carrier emissions $\text{PLI}(\Delta N)$ are proportional to ΔN , the band-gap emission decay time τ can be related to the defect lifetime by the relation

$$\tau_2 = (\Delta N + n_0)/\Delta N\tau. \quad (23)$$

This relation confirms the similarity of the decay times at band edge and at defect 2. The fits corresponding to the decay times of PL due to defects are shown in Figs. 5(e) and 5(f). The fits well coincide in a wide temperature range, indicating that these defects are active in recombination. The temperature dependence of PL_2 was fitted as $\text{PL}_2 = f_h$, i.e., it is only impacted by hole activation from quantum wells [Fig. 4(a)]. At low excitation defect 2 is only partially filled due to the concurrent capture to defect 1 (and the strong deficiency of holes at low temperatures, due to the dominance of excitons). Thus the slope of PL_2 is larger than unity at low excitations and temperatures. For temperature ranging between 80 and 150 K and under the lowest excitation, the hole density is very low ($<10^{15} \text{ cm}^{-3}$). Then the defect 2 emission at lowest excitations is very weak and this allows us to evaluate by Eq. (22) the vacancy concentration at $N_T = 5 \times 10^{15} \text{ cm}^{-3}$. At higher excitations the density of holes captured to defect 2 saturates to the density of the trap, leading to the linear slope, similarly as for defect 1. The filling mechanism of defect 2 with holes was much faster thus we could not resolve it experimentally. The hole lifetime of 40 ps at RT [Eq. (16)] provides, according to relation $\tau_h = 1/\sigma v_{th} N_T$, the value of the temperature-independent hole capture cross section of the aluminum vacancy $\sigma = 7 \times 10^{-13} \text{ cm}^2$ which confirms the behavior as a deep defect. The value of the capture cross section is lower for electrons: $1.5 \times 10^{-13} \text{ cm}^2$ according to Eq. (16). In GaN similar vacancy capture cross sections for holes 10^{-13} – 10^{-12} cm^2 were determined [65]. In

aluminum nitride similar $\sim 10^{16} \text{ cm}^{-3}$ vacancy concentrations were determined [66], while vacancy complex concentrations were by an order of magnitude larger, well coinciding with our findings.

D. Impact of dislocations to recombination

The nonradiative centers in Si-doped AlGaN alloys are attributed to Al vacancies [37]. Thus pure AlN exhibits a short 40-ps exciton lifetime in the 50–250-K range [67], whereas GaN exhibits dislocation-limited lifetimes a few orders of magnitude larger, ~ 0.5 – 24 ns [68]. Therefore, both defects can be active in AlGaN alloys. The evolutions of the PL efficiencies with temperature and versus excitation density in the AlGaN epilayer and in the MQW structure pointed out that exciton confinement in QWs is similar. Nevertheless, the gradual decrease of both the TIPL efficiency η_{PL} and of the initial lifetime τ_{PL} at high excitations requires deeper analysis of the mechanisms responsible for these effects, i.e., possible impact of diffusion coefficient [69].

The LITG decay kinetics were measured at two grating periods, 1.95 and 7.8 μm [Fig. 6(a)]. The measurements allowed us to determine simultaneously the carrier lifetime (τ) and the diffusion coefficient (D) against the excess carrier density. In the $\text{Al}_{0.61}\text{Ga}_{0.39}\text{N}/\text{Al}_{0.70}\text{Ga}_{0.3}\text{N}$ MQWs, at high photoexcitations (in the range from 0.1 to 1 mJ/cm^2), a sub-linear decrease of the carrier lifetime with increase of excess carrier density was observed and was described by a power law $\tau \propto \Delta N^{-(0.4 \pm 0.2)}$ in the 80–400-K range. The PL decay time in the $\text{Al}_{0.68}\text{Ga}_{0.32}\text{N}$ layer followed similar dependencies [see Figs. 3(c) and 3(d)]. On the contrary, the values of the diffusion coefficient D increased with excitation. A quadratic slope is measured [inset in Fig. 6(a)], which is typical for diffraction efficiency, but the observed slope value is reduced above 1 mJ/cm^2 , which can be explained by the increase of the recombination rates due to the degenerate plasma of carriers and to some possible amplified spontaneous emission [70,71]. The shift of the decay of the peak of diffraction

efficiency (DE) to earlier delay times and its symmetric shape at 2 mJ/cm² excitations indicates that, at these conditions, the lifetime is shorter than the laser pulse (20 ps).

In Fig. 6(b) is shown the inverse correlation between the diffusion coefficient and the lifetime. We note that a similar correlation was observed in bulk GaN with an nonhomogeneous distribution of growth defects, where the temperature-dependent diffusive flow of excess carriers to dislocations at hexagon grain boundaries governed the nonradiative recombination rate, $1/\tau_{\text{nonrad}} \sim D(T)$ [68]. Using for the recombination lifetime on dislocations equation [72]

$$\tau_d = \frac{1}{2\pi N_{\text{dis}} D} \left[-\ln(r_{\text{dis}} N_{\text{dis}}^{1/2}) - 0.5 \ln(\pi) - 0.077 \right] + \frac{1}{2\pi r_{\text{dis}} v_{\text{th}} N_{\text{dis}}}, \quad (24)$$

where r_{dis} is the dislocation radius, N_{dis} is dislocation density. In our samples, $N_{\text{dis}} = 1.5 \times 10^9 \text{ cm}^{-2}$.

We fit the lifetime and the diffusivity correlation as follows:

$$1/\tau = 1/\tau_{\text{nr}} + 1/\tau_d, \quad (25)$$

where τ_{nr} is vacancy limited lifetime as described above. The fit provides a dislocation radius of 12 nm in the AlGaIn layer and 15 nm in the MQWs. Equation (25) well describes the correlation between the inverse lifetime and the diffusion coefficient. The second term in Eq. (24) is much smaller; 7 ps ($v_{\text{the}} = (8kT/\pi m_e)^{0.5} = 10^7 \text{ cm/s}$ is the thermal velocity of electrons, considering that LITG monitors mainly electrons: $DE \sim 1/m_e + 1/m_h \sim 1/m_e$), and can only cause slight deviations leading to slightly sublinear correlation slope.

Threading dislocations (TDs) are of a dipolar nature (electrons and holes are localized on different sides of dislocations) [73], therefore they are observed as dark spots in cathodoluminescence imaging [74]. The modeling in GaN provide for dislocations similar Coulomb diameters of few tens of nanometers, while excitons are dissociated near dislocations thus diminishing the photoluminescence efficiency near the dislocations in by order of magnitude larger distances [75]. The barrier against carrier capture to dislocations can be screened by excited carriers. Therefore, at low excitation densities, making the correlation between the quantum efficiency and the dark spot density cannot be straightforward. Increasing the Si doping leads to observing an increase of the external quantum efficiency (EQE), which can be explained by the enhanced exciton formation with doping [see Eq. (2)], while that process saturates at high exciton density and then the EQE drops, plausibly due to a lifetime reduction by the TDs [74]. Moreover, recently a reduction of TD density with Si doping [76] similarly caused increase of the EQE.

The mobility of electrons in AlGaIn is 120 cm²/V/s [24] at RT, proving, according to the Einstein relationship, an electron diffusivity coefficient $D_e = 3 \text{ cm}^2/\text{s}$. For holes the corresponding value $\mu_h = 15 \text{ cm}^2/\text{V/s}$ [77], which allows us to calculate the hole diffusivity coefficient $D_h = 0.4 \text{ cm}^2/\text{s}$. The electron mobility is much larger according to ambipolar diffusion relation $D_a = 2D_e D_h / (D_e + D_h) \sim 2D_h$. At room temperature D_a equals 0.7 cm²/s. This value is close to that we determine at high excitation densities, indicating that at these conditions, localized states are fully filled and free-

carrier transport dominates (holes are weakly degenerate due to large mass, thus the increase of D would not appear due to their degeneracy). Indeed, at low excitations carrier transport should be hindered as localized excitons and carriers are immobile. This almost freezing of carriers correlates with the large values of lifetime, as they do not reach dislocations and they recombine radiatively or they recombine on the vacancies.

Therefore, the correlation between D and $1/\tau$ at high excitations pointed out the increased nonradiative recombination rate of delocalized carriers, as the delocalization was confirmed by the increasing value of D . The nonradiative recombination rate can be expressed by the equation $1/\tau_{\text{nonrad}} \sim (\Delta N_{\text{deloc}}/\Delta N)$ [57], where ΔN_{deloc} and ΔN_{loc} are the delocalized and localized carrier density, and where the total photoexcited carrier density is $\Delta N = \Delta N_{\text{deloc}} + \Delta N_{\text{loc}}$. The diffusion coefficient can be expressed as $D = D_0(\Delta N_{\text{deloc}}/\Delta N)$, where D_0 is the delocalized carrier diffusion coefficient. Therefore, both D and $1/\tau$ values increase with carrier delocalization and explain the experimental dependence $D \sim 1/\tau$ at high excitations [Fig. 6(b)].

Therefore, the drop of PL efficiency due to exciton dissociation occurs in AlGaIn at excitations above $2 \times 10^{18} \text{ cm}^{-3}$ and for temperatures $T > 150 \text{ K}$ (which are the actual conditions for UV LED operation), but at excitations above 10^{19} cm^{-3} the enhancement of recombination of free carriers on dislocations generate efficient additional drop mechanism. This should be managed and cured as it is limiting the performances of AlGaIn-based UV lasers.

IV. CONCLUSIONS

In conclusion, by using both temporal and spatial modulation of excess carrier densities and by monitoring their decays, we could determine the variations of carrier lifetimes in Al-rich AlGaIn layer and MQWs at temperatures ranging up to 550 K in a broad range of photoexcitation densities. The experimental results were analyzed within the framework of the same formalism for both structures as the layer consisted of a spontaneously formed superlattice. The radiative recombination was found dominant up to 150 K providing exciton lifetimes of 0.9–2.8 ns at excitation densities of about 1–10 $\mu\text{J}/\text{cm}^2$. The slight increase of the quantum efficiency at the lowest excitation densities was attributed to the filling of vacancy-oxygen complexes ($V_{\text{III}}\text{-}3\text{O}_{\text{N}}$). Further increasing the excitation density provoked a drop of the PL efficiency in relation with a decrease of the lifetime of carriers (down to $\sim 170 \text{ ps}$) in correlation with the excitonic dissociation and the subsequent enhanced recombination of holes on aluminum vacancies. Even at higher excitation densities, the delocalization of carriers, revealed by the diffusivity increase, enhanced diffusive recombination on dislocations. The modeling of the quantum efficiency and of PL decays versus temperature and excitation density provided values of exciton binding energies of 104 and 140 meV in the MQWs and in the AlGaIn layer respectively; exciton and carrier radiative recombination rate coefficients of $r_{\text{ex}} = (0.6 \pm 0.2) \times 10^9 \times (T/300)^{-1} \text{ s}^{-1}$ and $B_{\text{rad}} = (7 \pm 1) \times 10^{-10} \times (T/300)^{-3/2} \text{ cm}^3/\text{s}$, respectively. The localization energies for excitons are found in the 12- to 35-meV range, and the lifetime of localized exciton

varied in the interval between 2 and 4 ns. The modeling of the nonradiative recombination rate provided the capture rates for the vacancies and for the dislocations. The vacancy complex capture cross sections for excitons was determined to be $\sigma = (2 \pm 1) \times 10^{-16} \times (300/T)^2 \text{ cm}^2$. Electron and hole capture cross sections to aluminum vacancy were also obtained as $(1.5 \pm 1) \times 10^{-13} \text{ cm}^2$ and $(7 \pm 1) \times 10^{-13} \text{ cm}^2$, respectively. The Coulombic dislocation radius for free-carrier recombination was found to be 12–15 nm. This complete set of parameters is of paramount importance for designing aluminum-rich devices.

ACKNOWLEDGMENTS

The research was supported by the Research Council of Lithuania under the project No. S-MIP-19-34. This work was partially supported by MEXT in Japan, “Program for Building Regional Innovation Ecosystem,” JSPS KAKENHI Grant No. JP16H06415, and JST CREST Grant No. 16815710. B.G. acknowledges the financial support of the network GaNeX (ANR-11-LABX-0014). GaNeX belongs to the publicly funded Investissements d’Avenir program managed by the French ANR agency.

-
- [1] N. Ryškevič, S. Juršėnas, P. Vitta, E. Bakienė, R. Gaska, and A. Žukauskas, *Sens. Actuators, B* **148**, 371 (2010).
- [2] Z. Luksiene and L. Brovko, *Food Eng. Rev.* **5**, 185 (2013).
- [3] M. Shur, M. Shatalov, A. Dobrinsky, and R. Gaska, *Springer Ser. Mater. Sci.* **156**, 83 (2012).
- [4] M. Kneissl and J. Rass, *III-Nitride Ultraviolet Emitters* (Springer International, Cham, 2016).
- [5] A. Rodger, *Encyclopedia of Biophysics* (Springer, Berlin, 2013).
- [6] M. Kneissl, T. Y. Seong, J. Han, and H. Amano, *Nat. Photon.* **13**, 233 (2019).
- [7] <http://mercuryconvention.org/>.
- [8] Z.-H. Zhang, S.-W. Huang Chen, C. Chu, K. Tian, M. Fang, Y. Zhang, W. Bi, and H.-C. Kuo, *Nanoscale Res. Lett.* **13**, 122 (2018).
- [9] T. Y. Wang, C. T. Tasi, C.-F. Lin, and D.-S. Wu, *Sci. Rep.* **7**, 14422 (2017).
- [10] K. C. Shen, C. Hsieh, Y. J. Cheng, and D. P. Tsai, *Nano Energy* **45**, 353 (2018).
- [11] R. K. Mondal, V. Chatterjee, and S. Pal, *Physica E (Amsterdam, Neth.)* **108**, 233 (2019).
- [12] C. G. Moe, S. Sugiyama, J. Kasai, J. R. Grandusky, and L. J. Schowalter, *Phys. Status Solidi A* **215**, 1700660 (2018).
- [13] M. A. Khan, T. Matsumoto, N. Maeda, N. Kamata, and H. Hirayama, *Jpn. J. Appl. Phys.* **58**, SAA01 (2019).
- [14] T. Takayoshi, M. Takuya, S. Jun, N. Norimichi, T. Kenji, and H. Hideki, *Appl. Phys. Express* **10**, 31002 (2017).
- [15] K. B. Nam, J. Li, M. L. Nakarmi, J. Y. Lin, and H. X. Jiang, *Appl. Phys. Lett.* **81**, 1038 (2002).
- [16] H. Murotani, D. Akase, K. Anai, Y. Yamada, H. Miyake, and K. Hiramatsu, *Appl. Phys. Lett.* **101**, 42110 (2012).
- [17] S. Kurai, F. Ushijima, Y. Yamada, H. Miyake, and K. Hiramatsu, *Jpn. J. Appl. Phys.* **52**, 08JL07 (2013).
- [18] S. F. Chichibu, H. Miyake, Y. Ishikawa, M. Tashiro, T. Ohtomo, K. Furusawa, K. Hazu, K. Hiramatsu, and A. Uedono, *J. Appl. Phys.* **113**, 213506 (2013).
- [19] P. Lefebvre, C. Brimont, P. Valvin, B. Gil, H. Miyake, and K. Hiramatsu, *Phys. Status Solidi A* **211**, 765 (2014).
- [20] S. M. Sadaf, S. Zhao, Y. Wu, Y. H. Ra, X. Liu, S. Vanka, and Z. Mi, *Nano Lett.* **17**, 1212 (2017).
- [21] W. Yang, Y. Zhao, Y. Wu, X. Li, Z. Xing, L. Bian, S. Lu, and M. Luo, *J. Cryst. Growth* **512**, 213 (2019).
- [22] J. Mickevičius, G. Tamulaitis, M. Shur, M. Shatalov, J. Yang, and R. Gaska, *Appl. Phys. Lett.* **101**, 211902 (2012).
- [23] P. Ščaje, S. Miasojedovas, K. Jarašiunas, K. Hiramatsu, H. Miyake, and B. Gil, *Phys. Status Solidi B* **252**, 1043 (2015).
- [24] Y. Shimahara, H. Miyake, K. Hiramatsu, F. Fukuyo, T. Okada, H. Takaoka, and H. Yoshida, *Jpn. J. Appl. Phys.* **50**, 095502 (2011).
- [25] T. Suzuki, H. Yaguchi, H. Okumura, Y. Ishida, and S. Yoshida, *Jpn. J. Appl. Phys.* **39**, L497 (2000).
- [26] P. B. Klein, R. Myers-Ward, K. K. Lew, B. L. Vanmil, C. R. Eddy, D. K. Gaskill, A. Shrivastava, and T. S. Sudarshan, *J. Appl. Phys.* **108**, 033713 (2010).
- [27] K. Jarašiunas, S. Nargelas, R. Aleksiejunas, S. Miasojedovas, M. Vengris, S. Okur, H. Morkoç, Ü. Özgür, C. Giesen, Ö. Tuna, and M. Heuken, *J. Appl. Phys.* **113**, 103701 (2013).
- [28] P. Ščaje, M. Karaliunas, E. Kuokštis, and K. Jarašiunas, *J. Lumin.* **134**, 588 (2013).
- [29] S.-W. Feng, T.-Y. Tang, Y.-C. Lu, S.-J. Liu, E.-C. Lin, C. C. Yang, K.-J. Ma, C.-H. Shen, L. C. Chen, K. H. Kim, J. Y. Lin, and H. X. Jiang, *J. Appl. Phys.* **95**, 5388 (2004).
- [30] D. Watson-Parris, M. J. Godfrey, P. Dawson, R. A. Oliver, M. J. Galtrey, M. J. Kappers, and C. J. Humphreys, *Phys. Rev. B* **83**, 115321 (2011).
- [31] M. Shahmohammadi, G. Jacopin, G. Rossbach, J. Levrat, E. Feltin, J. F. Carlin, J. D. Ganière, R. Butté, N. Grandjean, and B. Deveaud, *Nat. Commun.* **5**, 1 (2014).
- [32] L. J. B. Gao, Min, S. T. Bradley, Yu Cao, D. Jena, Y. Lin, S. A. Ringel, J. Hwang, and W. J. Schaff, *J. Appl. Phys.* **100**, 103512 (2006).
- [33] G. A. Garrett, A. V. Sampath, H. Shen, M. Wraback, W. Sun, M. Shatalov, X. Hu, J. Yang, Y. Bilenko, A. Lunev, M. S. Shur, R. Gaska, J. R. Grandusky, and L. J. Schowalter, *Phys. Status Solidi Curr. Top. Solid State Phys.* **7**, 2390 (2010).
- [34] J. Mickevičius, J. Jurkevičius, K. Kazlauskas, A. Žukauskas, G. Tamulaitis, M. S. Shur, M. Shatalov, J. Yang, and R. Gaska, *Appl. Phys. Lett.* **101**, 041912 (2012).
- [35] B. Bastek, F. Bertram, J. Christen, T. Hempel, A. Dadgar, and A. Krost, *Appl. Phys. Lett.* **95**, 032106 (2014).
- [36] S. Nakamura, J. S. Speck, U. K. Mishra, S. P. Denbaars, T. Onuma, and S. F. Chichibu, *J. Appl. Phys.* **105**, 054501 (2013).
- [37] A. Uedono, K. Tenjinbayashi, T. Tsutsui, Y. Shimahara, H. Miyake, K. Hiramatsu, N. Oshima, R. Suzuki, and S. Ishibashi, *J. Appl. Phys.* **111**, 013512 (2012).
- [38] E. A. Shevchenko, V. N. Jmerik, A. M. Mizerov, A. A. Sitnikova, S. V. Ivanov, and A. A. Toropov, *Semiconductors* **46**, 998 (2012).

- [39] L. Hahn, F. Fuchs, L. Kirste, R. Driad, F. Rutz, T. Passow, K. Köhler, R. Rehm, and O. Ambacher, *Appl. Phys. Lett.* **112**, 151102 (2018).
- [40] N. Nepal, J. Li, M. L. Nakarmi, J. Y. Lin, and H. X. Jiang, *Appl. Phys. Lett.* **87**, 242104 (2005).
- [41] Z. Li, L. Wang, L. Jiu, J. Bruckbauer, Y. Gong, Y. Zhang, J. Bai, R. W. Martin, and T. Wang, *Appl. Phys. Lett.* **110**, 091102 (2017).
- [42] F. Scholz and F. Scholz, *Optical Processes in Semiconductors: Optical Spectroscopy* (Dover, New York, 2017).
- [43] P. Ščajev, J. Jurkevičius, J. Mickevičius, K. Jarašiūnas, and H. Kato, *Diam. Relat. Mater.* **57**, 9 (2015).
- [44] P. Ščajev, D. Litvinas, G. Kreiza, S. Stanionyte, T. Malinauskas, R. Tomašiūnas, and S. Juršenas, *Nanotechnology* **30**, 345702 (2019).
- [45] J. Gon Kim, A. Kimura, Y. Kamei, N. Hasuike, H. Harima, K. Kisoda, Y. Shimahara, H. Miyake, and K. Hiramatsu, *Appl. Phys. Lett.* **99**, 251904 (2011).
- [46] S. Schöche, P. Kühne, T. Hofmann, M. Schubert, D. Nilsson, A. Kakanakova-Georgieva, E. Janzén, and V. Darakchieva, *Appl. Phys. Lett.* **103**, 212107 (2013).
- [47] M. Suzuki and T. Uenoyama, *J. Appl. Phys.* **80**, 6868 (1996).
- [48] G. Bastard, E. E. Mendez, L. L. Chang, and L. Esaki, *Phys. Rev. B* **26**, 1974 (1982).
- [49] M. Yoshikawa, M. Kunzer, J. Wagner, H. Obloh, P. Schlotter, R. Schmidt, N. Herres, and U. Kaufmann, *J. Appl. Phys.* **86**, 4400 (1999).
- [50] B. Zhang, S.S. Kano, Y. Shiraki, and R. Ito, *Phys. Rev. B* **50**, 7499 (1994).
- [51] J. Fu, T. Song, X. Liang, and G. Zhao, *Results Phys.* **14**, 102505 (2019).
- [52] D. M. Graham, A. Soltani Vala, P. Dawson, M. J. Godfrey, M. J. Kappers, T. M. Smeeton, J. S. Barnard, C. J. Humphreys, and E. J. Thrush, *Phys. Status Solidi B* **240**, 344 (2003).
- [53] G. Bourdon, I. Robert, I. Sagnes, and I. Abram, *J. Appl. Phys.* **92**, 6595 (2002).
- [54] P. Ščajev, R. Aleksiejunas, S. Miasojedovas, S. Nargelas, M. Inoue, C. Qin, T. Matsushima, C. Adachi, and S. Juršenas, *J. Phys. Chem. C* **121**, 21600 (2017).
- [55] W. Shockley and W. T. Read, *Phys. Rev.* **87**, 835 (1952).
- [56] D. Rosales, B. Gil, T. Bretagnon, B. Guizal, F. Zhang, S. Okur, M. Monavarian, N. Izyumskaya, V. Avrutin, U. Özgür, H. Morkoç, and J. H. Leach, *J. Appl. Phys.* **115**, 073510 (2014).
- [57] B. K. Ridley, *Quantum Processes in Semiconductors* (Clarendon, Oxford, 1999).
- [58] M. Winkelnkemper, M. Dworzak, T. P. Battel, A. Strittmatter, A. Hoffmann, and D. Bimberg, *Phys. Status Solidi B* **245**, 2766 (2008).
- [59] F. Wu, J. Zhang, S. Wang, H. Long, J. Dai, Z. C. Feng, Z. Gong, and C. Chen, *Opt. Mater. Express* **5**, 2608 (2015).
- [60] L. Béaur, T. Bretagnon, B. Gil, A. Kavokin, T. Guillet, C. Brimont, D. Tainoff, M. Teisseire, and J. M. Chauveau, *Phys. Rev. B* **84**, 165312 (2011).
- [61] C. Himwas, R. Songmuang, Le Si Dang, J. Bleuse, L. Rapenne, E. Sarigiannidou, and E. Monroy, *Appl. Phys. Lett.* **101**, 241914 (2012).
- [62] M. E. Rudinsky and S. Y. Karpov, *Phys. Status Solidi A*, 1900878 (2019), doi:10.1002/pssa.201900878.
- [63] P. Ščajev, S. Miasojedovas, L. Subačius, K. Jarašiūnas, A. V. Mazanik, O. V. Korolik, and M. Kato, *J. Lumin.* **212**, 92 (2019).
- [64] B. Borisov, V. Kuryatkov, Y. Kudryavtsev, R. Asomoza, S. Nikishin, D. Y. Song, M. Holtz, and H. Temkin, *Appl. Phys. Lett.* **87**, 132106 (2005).
- [65] H. Yamada, H. Chonan, T. Takahashi, T. Yamada, and M. Shimizu, *AIP Adv.* **8**, 045311 (2018).
- [66] Y. Kanechika, Y. Horii, M. Azuma, and H. Fukushima, *Trans. Mater. Res. Soc. Jpn.* **40**, 95 (2015).
- [67] K. B. Nam, J. Li, M. L. Nakarmi, J. Y. Lin, and H. X. Jiang, *Appl. Phys. Lett.* **82**, 1694 (2003).
- [68] P. Ščajev, A. Usikov, V. Soukhoveev, R. Aleksiejūnas, and K. Jarašiūnas, *Appl. Phys. Lett.* **98**, 202105 (2011).
- [69] R. Aleksiejunas, K. Gelžinyte, S. Nargelas, K. Jarašiūnas, M. Vengris, E. A. Armour, D. P. Byrnes, R. A. Arif, S. M. Lee, and G. D. Papanoulitis, *Appl. Phys. Lett.* **104**, 022114 (2014).
- [70] P. Ščajev, C. Qin, R. Aleksiejunas, P. Baronas, S. Miasojedovas, T. Fujihara, T. Matsushima, C. Adachi, and S. Juršenas, *J. Phys. Chem. Lett.* **9**, 3167 (2018).
- [71] J. Mickevičius, J. Jurkevičius, K. Kazlauskas, A. Žukauskas, G. Tamulaitis, M. S. Shur, M. Shatalov, J. Yang, and R. Gaska, *Appl. Phys. Lett.* **100**, 081902 (2012).
- [72] C. Donolato, *J. Appl. Phys.* **84**, 2656 (1998).
- [73] S. L. Rhode, M. K. Horton, W. Y. Fu, S. L. Sahonta, M. J. Kappers, T. J. Pennycook, C. J. Humphreys, R. O. Dusane, and M. A. Moram, *Appl. Phys. Lett.* **107**, 243104 (2015).
- [74] S. Kurai, K. Anai, H. Miyake, K. Hiramatsu, and Y. Yamada, *J. Appl. Phys.* **116**, 235703 (2014).
- [75] V. M. Kaganer, J. Lähnemann, C. Pfüller, K. K. Sabelfeld, A. E. Kireeva, and O. Brandt, *Phys. Rev. Appl.* **12**, 054038 (2019).
- [76] C. He, Z. Qin, F. Xu, M. Hou, S. Zhang, L. Zhang, X. Wang, W. Ge, and B. Shen, *Sci. Rep.* **5**, 1 (2015).
- [77] J. Simon, V. Protasenko, C. Lian, H. Xing, and D. Jena, *Science* **327**, 60 (2010).